Analytical Methods

Check for updates

A nitrogen-doped carbon nanosheet/poly(amidoamine) dendrimer-based electrochemical sensor for nicotine in flavored hookah pipe tobacco†

Sesethu Makaluza,[ab] Nyasha Midzi,[ab] Foluke O. G. Olorundare,[a] Dimpo S. Sipuka,[ab] Tsholofelo I. Sebokolodi,[ab] Duduzile Nkosi[ab] and Omotayo A. Arotiba [ID] *[ab]

Towards the nicotine addiction challenge in the smoking of hookah pipe products, we hereby present the development of an electrochemical sensor for nicotine detection. A nitrogen-doped carbon nanosheet (N-CNS)/poly(amidoamine) dendrimer (PAMAM) nanocomposite-modified electrode was prepared as a sensor for the detection of nicotine in analytical and real samples. The N-CNSs were prepared by a hydrothermal method and dropcast on a glassy carbon electrode followed by electro-deposition of the PAMAM dendrimer to form the sensor (GCE/N-CNSs/PAMAM). The N-CNSs were characterized with electron microscopy, Raman spectroscopy and FTIR. The sensor was characterized with voltammetry and electrochemical impedance spectroscopy. The N-CNS/PAMAM enhanced the electrochemical performance of the electrode towards the oxidation of nicotine. The sensor achieved a detection limit of 0.05 μM in a linear concentration range of 1.93–61.64 μM nicotine standard samples. The sensor showed good reproducibility, repeatability, and selectivity. The sensor was successful in selectively detecting nicotine in two local brands of hookah pipe tobacco with a 113–121 percent recovery. Nicotine, up to a concentration of 0.35–0.39 mg g^{-1}, was found in the sampled hookah pipe tobacco products suggesting possible harm to human health.

1. Introduction

Tobacco smoking, which poses a threat to human health, has been made fashionable through various modes such as vaping/e-cigarettes, shisha/hookah pipe, and other tobacco products.[1] The popularity of hookah pipe tobacco is due to the misconception that it is a safer nicotine-delivery system compared to the direct puffing of the combusted smoke of filtered cigarettes.[2] This perception comes from the fact that the charcoal-combusted smoke first goes through the water bowl that is part of the hookah pipe device, and users believe that the charcoal and the bubbling trap some toxins in the smoke before it is inhaled.[3] The prevalence of hookah pipe tobacco smoking can also be attributed to the flavouring of these shisha products with natural, aromatic, and appealing flavouring agents such as menthol, vanilla, apple, cherry, and others.[4] Another factor that cannot be ignored is that hookah sessions are associated with an "aesthetic" lifestyle, otherwise casually known as 'soft life'

amongst young people, as they usually enjoy hookah at places like restaurants, clubs, hotels, *etc.*[5] Because these sessions are 45 minutes or longer, and the presence of volatile compounds in these products has the potential to carry over higher nicotine concentration, hookah pipe tobacco consumption is reported to be more toxic and dangerous than cigarettes.[6]

The various chemicals in tobacco products are reported to be responsible for several fatal diseases like lung cancer, cardiovascular diseases (including abdominal aortic aneurysm and heart attack), cerebrovascular diseases (including stroke and brain aneurysm), *etc.*[7,8] These chemicals are also reported to have a negative impact on the life expectancy of people living with mental health disorders.[9] Amongst these chemicals, nicotine is of concern and of interest in this paper. There is a lack of thorough research to help regulatory authorities determine the exact quantity of ingredients in flavoured hookah pipe tobacco, particularly nicotine, to check these products accordingly. This gap highlights the need for simple and more efficient analytical methods that can assist both regulatory authorities and the health sector in monitoring nicotine levels in this unique sample matrix and among hookah smokers. Like cigarettes, which have been extensively studied where even electroanalytical techniques are widely applied, hookah pipe tobacco presents a new and unique challenge.

[a]Department of Chemical Sciences, University of Johannesburg, Doornfontein, 2028, South Africa. E-mail: oarotiba@uj.ac.za

[b]Centre for Nanomaterials Science Research, University of Johannesburg, South Africa
† Electronic supplementary information (ESI) available. See DOI: https://doi.org/10.1039/d4ay01257g

This study therefore proposes a novel nanocomposite electrochemical sensor to measure nicotine (the main cause of tobacco addiction) in flavoured hookah pipe tobacco.

Nicotine is a natural pyridine alkaloid, and its IUPAC name is 3-(1-methyl-2-pyrrolidinyl) pyridine.[10] It is used as a recreational drug for the relief of neuropsychiatric disorders such as anxiety, depression, attention deficit hyperactivity disorder (ADHD), *etc.*, which are associated with abnormally low levels of neurotransmitters such as serotonin and dopamine.[11] People with these disorders tend to have a high dependency on the drug, which raises a global concern, especially because of the tobacco fatalities mentioned earlier.[12] Nicotine addiction and dependency are attributed to the binding of nicotine to nicotinic receptors in the brain that are responsible for releasing dopamine.[13] Exposure to nicotine for longer hours or days means there is a high affinity of nicotinic receptors over time which in turn further induces the release of dopamine, giving a pleasurable sense of elation, improved memory, and reduced anxiety.[7,14] These are temporary solutions to health problems and are outweighed by the adverse health issues caused by the constant need to smoke. This also then facilitates the need for simple, user-friendly, and low-cost methods of quantifying nicotine.[15,16]

Several analytical methods of detecting nicotine in diverse types of sample matrices exist. Separation techniques like high-performance liquid chromatography (HPLC), capillary electrophoresis (CE), gas chromatography (GC), and liquid chromatography (LC) are the most common methods for hookah flavour because of their reliability, accuracy, and specificity.[17,18] Hyphenated techniques (such as GC-mass spectroscopy (MS), GC-flame ionization detector (FID), LC-MS, CE-MS, *etc.*) are mostly preferred to enhance the detection of nicotine.[2,4] These techniques, however, have limitations as they are expensive, sophisticated, require skilled technicians, and are too large to be used for onsite application.[19] Electrochemical sensors are good analytical tools for the detection of various compounds, including nicotine, because of their simplicity, low cost, selectivity, and fast response, among their many advantages.[20] Lee and Woi reported an electrochemical sensor based on rGO/CuHCF for the determination of nicotine in e-cigarettes. The sensor achieved a limit of detection of 0.026 μM in the concentration range of 0.035–5 mM.[21] Sridharan *et al.* developed an electrochemical sensor for nicotine in human saliva based on green synthesised silver nanoparticles, with a limit of detection of 0.135 μM (in the concentration range of 2.5–105 μM).[22] Sebokolodi *et al.* demonstrated a carbon nanofiber-poly(amidoamine) dendrimer-based electrochemical sensor for the detection of nicotine in cigarettes, obtaining a limit of detection of 0.02637 μM (in the concentration range of 0.4815–15.41 μM) in 0.1 M PBS at pH 7.5.[7] These reports show the importance of nanomaterials in the development of sensors for nicotine.

The fabrication of bare electrodes with materials such as carbon nanomaterials and macromolecular structures like dendrimers has drawn significant interest in sensing in general because of their promising electrocatalytic activity, large surface area, unique structural morphologies, and amenable chemical compositions. These materials offer improvements in electrode fouling, poor sensitivity, stability, and selectivity.[23] PAMAM dendrimers, which can be built up from ethylene diamine or 1,4-diaminobutane cores with amine or acidic terminal groups, are extensively used in sensor development because of their biocompatibility, unique structural and morphological properties, and their chemical composition. Their dendritic architecture, nanocavities or voids, globular branches and multiple functional groups enhance the possibility of entrapment, supramolecular linking and host-guest chemistry making them highly effective in various sensor applications.[24,25]

In this study, nitrogen-doped carbon nanosheets (N-CNSs) provide improved surface area, conductivity, sensitivity, and selectivity of the bare glassy carbon electrode (GCE) towards nicotine detection. The incorporation of generation 4 PAMAM dendrimer, with the 1,4-aminobutane core and the succinamic acid (SAH) terminal group, further enhances these properties as inspired by the work of Sebokolodi *et al.*[7] The sensor was fabricated by drop-casting a thin layer of N-CNSs on a bare glassy carbon electrode (GCE), followed by immobilization of the poly(amidoamine) dendrimer (PAMAM) by electrodeposition. The sensor was then applied for nicotine detection in standard and flavoured hookah pipe tobacco samples. To our knowledge, this is a novel use of N-CNS/PAMAM as a composite platform for electrochemical sensors for nicotine.

2. Experimental

2.1. Materials

All purchased chemicals were of analytical grade: nicotine reference standard by Dr Ehrenstorfer was purchased from the LGC group (Germany). Caffeine and sodium hydroxide pellets were purchased from Sisco Research Laboratories (India). Sodium chloride, medium molecular weight chitosan, glacial acetic acid, sodium chloride, potassium ferricyanide(III), potassium hexacyanoferrate(II) trihydrate, potassium phosphate monobasic, potassium phosphate dibasic, potassium chloride, generation 4 poly(amidoamine)-succinamic acid dendrimer (PAMAM), ethanol, and acetonitrile were all purchased from Sigma Aldrich (South Africa). Ultrapure water was used throughout the work. Solutions of 0.1 M and 10 mM phosphate buffer saline were prepared from potassium phosphate (PBS) of pH 7.45 to prepare PAMAM, and 10 mM PBS (pH 7.45) was used to prepare nicotine standards and real samples.

2.2. Instrumentation

A Zeiss German 2 crossbeam 540 FESEM by Zeiss (Germany) and a Joe-JEM 2100F TEM by Joel Ltd (Japan) were employed for microscopic structure examinations. A DXR2 Smart Raman by Thermo Scientific (USA), an Alpha FTIR by Bruker (Germany), and an X'Pert Pro X-ray Diffractometer by Malvern Panalytical Ltd (UK) were employed for spectroscopic characterization. A three-electrode system was used with an Ivium compactstat potentiostat (The Netherlands), which included a GCE as the working electrode, a Ag/AgCl in 3 M NaCl as the reference electrode, and a platinum wire as the counter electrode, for all

electrochemical applications. The sensor's analytical performance was verified with UV-Vis spectrometry on a Cary 60 by Agilent Technologies.

2.3. Hydrothermal synthesis of nitrogen-doped carbon nanosheets (N-CNSs)

Nitrogen-doped carbon nanosheets were synthesised using an *in situ* method described by Qiao Liu,[26] and Maria K. Rybarczyk[27] with modification: a mass of 1 g chitosan was added into a mixture of 10 mL concentrated glacial acetic acid, 10 mL water, and 200 mg urea, in a 100 mL beaker. The mixture was homogenized by ultrasonication for 1 hour and transferred into a 100 mL Teflon-lined stainless-steel autoclave, and the reaction was conducted at 180 °C for 18 hours. The dark-brown product was then centrifuged for 15 minutes at 7700 rpm, and the resulting product was then dried in an oven at 80 °C for 24 hours.[26,27]
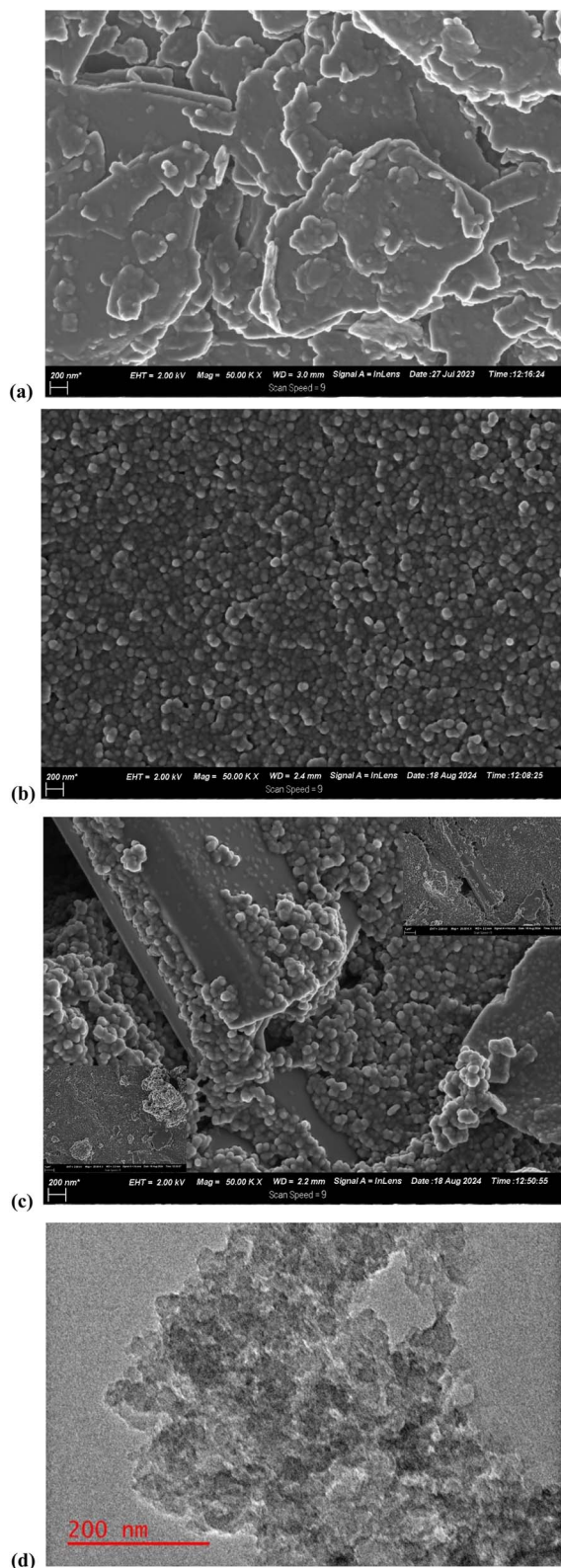

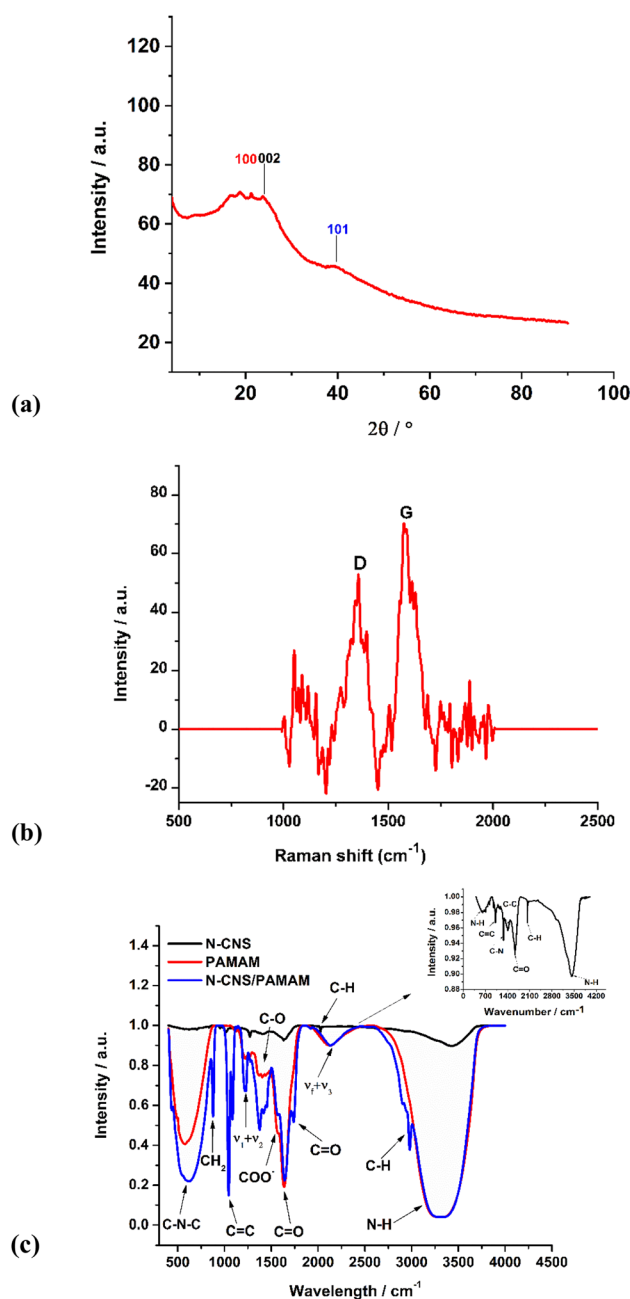Fig. 1 FESEM of (a) N-CNS, (b) PAMAM, and (c) N-CNS/PAMAM, and TEM of (d) N-CNSs.

Fig. 2 (a) XRD of N-CNSs, (b) Raman spectra of N-CNSs and (c) FTIR of N-CNS, PAMAM and N-CNS/PAMAM.

2.4. Fabrication of the electrode

A GCE was cleaned in succession with 1.00 μm, 0.3 μm, and 0.005 μm alumina polishing slurries. The electrode was then washed with water and ethanol using an ultrasonic bath for 2 minutes and left to dry overnight. About 10 mg of the dry N-CNSs were dispersed in 1 mL ethanol and sonicated for 1 hour for homogeneity. The sensor was prepared as follows: 5 μL of N-CNSs were dropcast on the surface of the clean GCE and air-dried (labelled GCE/N-CNSs). Then PAMAM was electro-deposited from its 10 mM solution using cyclic voltammetry on the GCE/N-CNSs forming the GCE/N-CNSs/PAMAM composite modified electrode – the final sensor. The CV parameters for electro-oxidation were set at −200 mV to 1400 mV, 50 mV s^{-1} for 30 cycles.

2.5. Electrochemical characterisation

Cyclic voltammetry (CV), differential pulse voltammetry (DPV), and electrochemical impedance spectroscopy (EIS) were used to characterise the electrodes in 5 mM $[Fe(CN)_6]^{-3/-4}$ with 0.1 M KCl (for CV and EIS) and 0.96 μM nicotine in 10 mM PBS (pH 7.45) for DPV. PBS (pH 7.45) is ideal for bio-sensing as it mimics the human body and is suitable for nicotine oxidation.[28,29] For CV, the parameters were set at the potential window of −200 mV to 700 mV, at 50 mV s^{-1} scan rate. For EIS, the bias potential was set at 200 mV at 100 kHz to 0.1 Hz frequencies and an amplitude of 10 mV. DPV parameters: potential window from −200 to 1200 mV, 20 ms pulse time, 140 mV pulse amplitude at 50 mV s^{-1}.

2.6. Salt-assisted extraction of nicotine from flavoured hookah pipe tobacco

A method by Aldeek *et al.* was used with modification to extract nicotine from flavoured hookah pipe tobacco. About 1 g of brand 1 and brand 2 flavoured hookah pipe tobacco were placed in separate 50 mL centrifuge tubes. NaOH (25 mL of 2 M) was added to each tube and a vortex mixer was used to shake the mixtures for 5 minutes. The mixtures were then homogenized using an ultrasonic bath for an hour. Acetonitrile (15 mL) and NaCl (1 g) were added, and mixing and homogenization were conducted in the same way as before. The contents were centrifuged for 15 minutes to separate the nicotine in the organic layer from the aqueous solution.[30] Each brand (2 mL) was diluted with 10 mM PBS (pH 7.45) in a separate 50 mL volumetric flask to prepare spiked and unspiked samples.

3. Results and discussion

3.1. Microscopic characterisation

Irregular-shaped sheets of N-CNSs, with a rough texture on the surface can be observed in the FESEM image (Fig. 1a). Fig. 1b
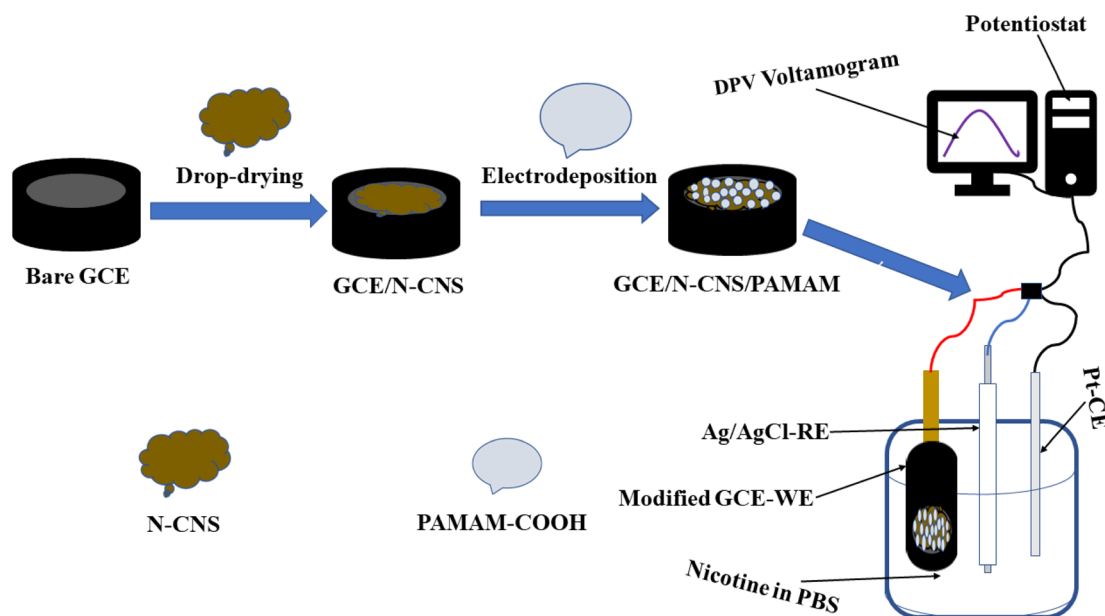
Scheme 1 Development of the GCE/N-CNS/PAMAM composite sensor for the detection of nicotine.

Table 1 Data from CV, DPV, and EIS of the modified and unmodified electrodes

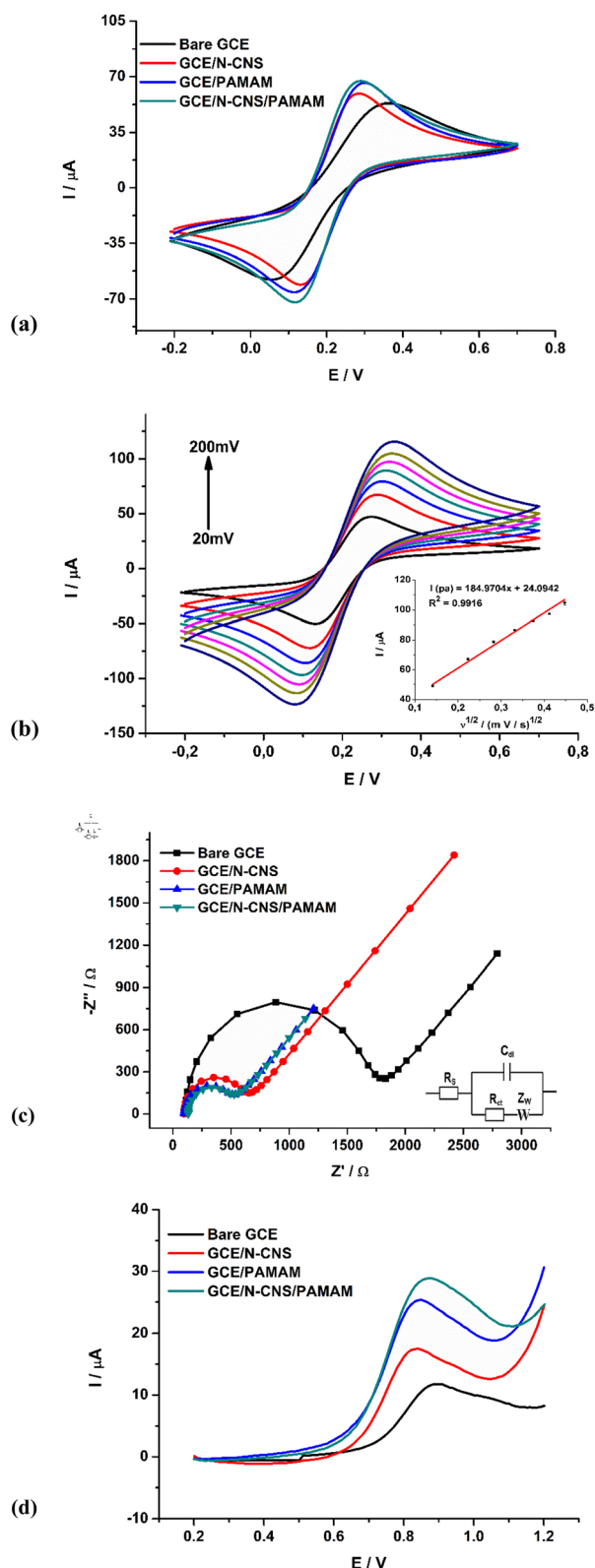| Electrode	CV (E_{pa})/mV	CV (I_{pa})/μA	DPV (E_{pa})/mV	DPV (I_{pa})/μA	EIS (R_{ct})/Ω
Bare GCE	360	46.35	900	13.12	1555
GCE/N-CNS	280	59.11	840	25.18	491.7
GCE/PAMAM	300	64.65	840	31.25	372.3
GCE/N-NCS/PAMAM	300	67.72	850	35.16	343.5

Fig. 3 (a) CV of bare and modified electrodes, (b) scan rate study (with the linear plot of $v^{1/2}$ vs. I_{pa}) of the nanocomposite sensor, (c) EIS of bare and modified electrodes in 5 mM ferri/ferrocyanide, and (d) DPV of bare and modified electrodes in 0.96 μM Nicotine.

shows the spherical structures of the PAMAM dendrimer with uniform size distribution. The FESEM image of the composite (N-CNS/PAMAM) (Fig. 1c) shows the spherical structures of PAMAM that are deposited in between and on top of the sheets (N-CNS). The TEM image (Fig. 1d) further shows the amorphous characteristics of the carbon material, visible by the phase contrast as well as the porous structure of the thin sheets.[31–33]

3.2. Spectroscopic characterisation

XRD, Raman, and FTIR were used to further explore the structural properties of the N-CNSs as seen in Fig. 2. The XRD spectrum (Fig. 2a) depicts the amorphous characteristics of the N-CNSs observed in the broad diffraction peak at around 20°. The diffraction peaks at 23°, 28°, and 40° can be assigned to the 100, 002, and 101 planes of the hexagonal lattice of N-CNSs, respectively. This indicates the formation of carbon nanosheets with high nitrogen content and porous structure.[31,34]

The characteristic peaks of the sp^2 carbon D-band and the sp^3 carbon G-band at 1350 cm^{-1} and 1580 cm^{-1}, respectively, can be observed in the Raman spectrum (Fig. 2b). The I_D/I_G ratio was calculated to be 0.77, which indicates a minor defect in the hexagonal lattice of the N-CNSs.[35]

The FTIR spectra (Fig. 2c) show an overlay of N-CNS (black line), PAMAM (red line), and N-CNS/PAMAM (blue line). For the N-CNS, absorption bands at 3418 cm^{-1}, 2026 cm^{-1}, 1632 cm^{-1}, 1405 cm^{-1}, 1271 cm^{-1}, 1021 cm^{-1}, and 619 cm^{-1}, which can be assigned to N–H stretching (primary amine), C–H bending (aromatic), C=N stretching (primary amine), C–C stretching (cyclic alkene), C–N stretching (tertiary amine), C=C stretching (cyclic alkene), and N–H wagging (aromatic), respectively, confirm the functional groups expected for a hexagonal lattice of aromatic amines and cyclo-alkenes in the N-CNS structure.

For PAMAM, absorption bands at 3316 cm^{-1}, 2133 cm^{-1}, 1637 cm^{-1}, 1564 cm^{-1}, 1395 cm^{-1}, 1229 cm^{-1}, and 576 cm^{-1} are assigned to the N–H stretching (primary & secondary amine), combination band $[v_f(v_1 + v_2) + v_3(CH_2)]$, C=O stretching (amide), N–H bending (amide 2 band), COO$^-$ stretching (carboxylic), C–O stretching (succinamic acid), and C–N–C out of plane bending (succinamic acid), respectively. These absorption bands confirm the functional groups expected for a PAMAM-G4-SAH structure with a 1,4-diaminobutane $[NH_2$-$(CH_2)_4$-$NH_2]$ core and the succinamic acid (NH$_2$-COCH$_2$CH$_2$-COOH) terminal. The amide groups are from within the branches of generation 4 PAMAM.[36]

For N-CNS/PAMAM, absorption bands at 3321 cm^{-1}, 2982 cm^{-1}, 2131 cm^{-1}, 1734 cm^{-1}, 1640 cm^{-1}, 1572 cm^{-1}, 1372 cm^{-1}, 1225 cm^{-1}, 1088 cm^{-1}, 1043 cm^{-1}, 879 cm^{-1}, and 601 cm^{-1}, are assigned to the N–H stretching (primary & secondary amine), C–H stretching (aliphatic) combination band $[v_f (v_1 + v_2) + v_3(CH_2)]$, [C=O stretching (carboxylic), C=O stretching (amide), N–H bending (amide 2 band), COO$^-$ stretching (carboxylic)], $v_1 + v_2$ [C–O stretching (succinamic acid) + C–N stretching (tertiary amine)], C=C stretching (cyclic alkene), CH$_2$ rocking (aliphatic), and C–N–C out of plane bending (succinamic acid), respectively. These absorption

bands confirm the functional groups expected for a N-CNS/PAMAM composite structure with combination peaks denoted as ν, observable by broadening of the peaks that were not expected or were ideally less intense in the fundamental peak positions of the materials.

3.3. Electrochemical characterisation

The GCE/N-CNS platform was achieved because of the possible interactions between the nucleophilic amines of the N-CNSs

Fig. 4 (a) DPV response of the GCE/N-CNS/PAMAM nanocomposite sensor in the linear concentration range of 0–61.64 μM nicotine in 10 mM PBS (pH = 7.45), and (b) the calibration curve of current response versus concentration (1.93–61.64 μM).

and the electrophilic, sp^2 hybridized carbon of the GCE, or π–π stacking between the olefinic groups of both.[37–41] Similarly, the GCE/PAMAM platform was achieved through the Michael-like addition of the primary amines of the dendrimer onto the GCE, assisted by electro-oxidation during electro-deposition, like in the self-assembly monolayer technique of depositing the organic material on the GCE.[41,42] The composite sensor GCE/N-CNS/PAMAM was achieved through possible acylation between the nucleophilic amines of N-CNSs and the electrophilic amides of PAMAM, amongst possible reactions, during electrodeposition.[43–45] Scheme 1 illustrates the fabrication process of the bare electrode to form a composite sensor and its DPV characterization in nicotine.

Table 1 details the data, while Fig. 3 exhibits the voltammograms obtained during electrochemical characterization. A shift to a less positive potential from the GCE to the modified electrodes was observed in CV (Fig. 3a), showing the effect of the modification. The partially positive amines in the N-CNSs facilitate the approach of the negatively charged ferri/ferrocyanide to the electrode interface by electrostatic attraction and the large surface area will accumulate more probes at the interface. These two phenomena will facilitate electron transfer and the increase in oxidation peak current. The shift to a lower potential also means oxidation and reduction of the ferri/ferrocyanide occurred at a lower energy of the modified electrodes. The GCE/PAMAM shows a more enhanced oxidation current than N-CNSs, and this can be because the primary amine groups in PAMAM at pH 7.45 are more positively charged than the mixture of primary and tertiary amines of N-CNSs.[46] The most enhanced oxidation current was observed for the nanocomposite (GCE/N-CNS/PAMAM) indicating a favourable combination of the two nanomaterials – N-CNS and PAMAM. EIS (Fig. 3b) shows a similar trend to the CV result – reduced R_{ct} is expected to have increased current (inverse relationship). From the EIS, the GCE and GCE/N-CNS/PAMAM show the highest and lowest charge transfer resistance (R_{ct}), respectively. The changes in R_{ct} are indicative of successful modification of the electrode. A reduced R_{ct} (Table 1) means that the interfacial reaction (transfer of charge) of the redox probe is more facile and can be indicative of improved electroactivity and conductivity of the modifier or platform. A scan rate study (Fig. 3c) was conducted to study the electrochemical kinetics of the
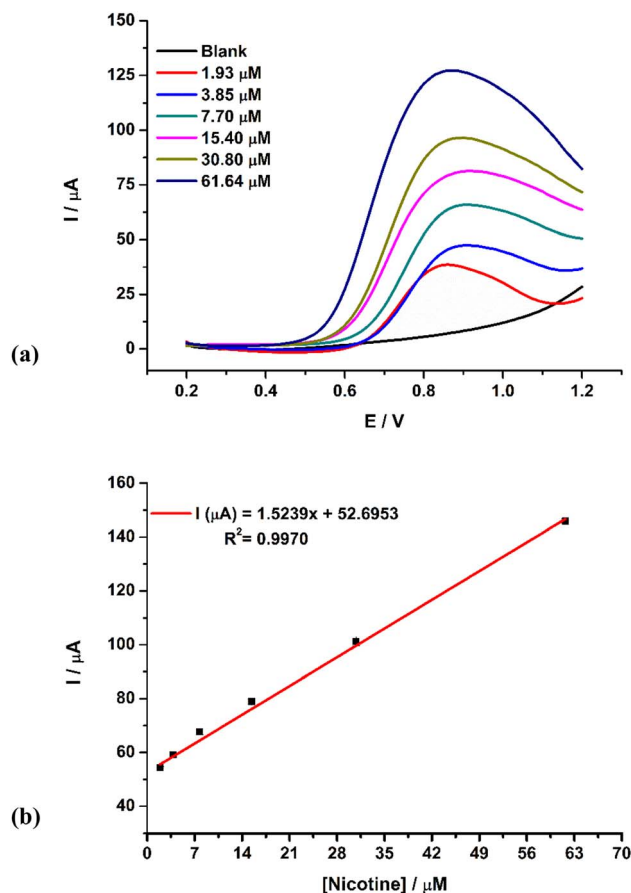
Table 2 Comparison of GCE/N-CNS/PAMAM with recently reported nicotine sensors[a]

Electrode	Detection method	Linear range	LOD	Sample type	References
FC/MWCNTs/SPCE	DPV	60–1000 μM	4.25 μM	Tobacco	50
pAzRS/PGE	DPV	0.25–100 μM	89 nM	HS, saliva	51
AgNPs/GCE	AMP	2.5–105 μM	0.135 μM	Saliva	52
AuNPs/GCE	AMP	0.02–280 μM	0.01 μM	HTP	53
Au/Chitosan/CPE	CA	4.0–320 μM	7.6 μM	Urine	54
MOF/GCE	SWV	0–50 μM	0.25 μM	Urine, cigarette	55
GCE/N-CNS/PAMAM	DPV	0–61.64 μM	0.05 μM	Hookah flavour	This work

[a] FC: ferrocene-functionalized, MWCNTs: multiwalled carbon nanotubes, SPCE: screen printed carbon electrode, pAzRS: poly azorubin s film, PGE: pencil graphite electrode, AgNPs: silver nanoparticles, AuNPs: gold nanoparticles, Au: gold, CPE: carbon paste electrode, MOF: metal organic frameworks, DPV: differential pulse voltammetry, AMP: amperometry. CA: chronoamperometry, SWV: square wave voltammetry.

nanocomposite sensor (GCE/N-CNS/PAMAM) in ferri/ferrocyanide. The oxidation current was observed to increase with increasing square root of the scan rate, and the correlation coefficient of 0.9919 in the linear insert plot proves that the redox reaction is diffusion-controlled, an attribute needed for the quantification of the analyte. The scan rate studies of the bare GCE, GCE/N-CNS, GCE/PAMAM, and GCE/N-CNS/PAMAM in 5 mM ferri/ferrocyanide were used to calculate the electrochemical active surface areas (ECSA) of the sensors, with the employment of the Randles–Sevcik equation ($m = 2.6910^5 \times A \times \sqrt{D} \times \sqrt[3]{n} \times C$), where m is the slope of $v^{1/2}$ vs. I_{pa}, A is the electrochemical active surface area (cm^2), D is the diffusion coefficient of the ferri/ferrocyanide (7×10^{-6} cm^2 s^{-1}), n is the number of electrons of ferri/ferrocyanide transferred ($1e^\bullet$), and C is the concentration of the ferri/ferrocyanide (5×10^{-6} mol cm^{-3}). The ECSA calculated was 0.1001, 0.1427, 0.1394, and 0.1573 cm^2 for the bare GCE, GCE/N-CNS, GCE/PAMAM, and GCE/N-CNS/PAMAM, respectively. The highest ECSA exhibited by the nanocomposite of N-CNS/PAMAM (the sensor) means that more electroactive sites are available for the redox reaction and this supports the highest current observed in the CV.

Further characterization of the sensors (modified electrodes) in the presence of nicotine shows the effect of the modifiers on the electro-oxidation of nicotine (Fig. 3d). DPV also follows the same trend as CV. The large surface area of the porous N-CNS with more π electrons and energy levels helps oxidize nicotine faster. Also, the positively charged amine groups of PAMAM at pH 7.45 are greater than those of nicotine at the same pH, enabling charge induction on nicotine and therefore attraction. Furthermore, the presence of N-CNS provides a platform for more π–π interaction with nicotine and this leads to better preconcentration of nicotine and therefore more molecules are available for electro-oxidation.[47,48] Like with CV, the highest current and the lowest oxidation peak potential occurred at the GCE/N-CNS/PAMAM. The combination of N-CNS and PAMAM shows better oxidation of nicotine than N-CNS and PAMAM as single materials, suggesting that the composition of these two is synergistic.[49]

3.4. Electrochemical detection of nicotine

The concentration study of the nanocomposite sensor (GCE/N-CNS/PAMAM) was carried out using DPV (Fig. 4a) in a linear concentration range of 1.93 to 61.64 μM nicotine and the blank was also analysed. An increase of current with increasing concentration was observed. The calibration curve (Fig. 4b) shows the linear relationship with a correlation coefficient of 0.9970 and a limit of detection of 0.05 μM, calculated using $\text{LOD} = \dfrac{3\sigma \text{ blank}}{\text{slope}}$. To determine the standard deviation of the blank used in calculating the limit of detection, DPV analysis using the composite sensor (GCE/N-CNS/PAMAM) in 10 mM PBS was conducted multiple times. The baseline current for the blank was measured each time. This was done by extrapolation of the baseline current at the potential where nicotine oxidation occurred for this sensor. The standard deviation was then

calculated from the extrapolated baseline current values, which was then used to calculate the LOD. The detection limit and concentration range of this sensor are in a similar range to (and better in some cases) some of the previously reported sensors for nicotine detection (Table 2).

3.5. Reproducibility, repeatability and selectivity of the sensor

The sensor was assessed for reproducibility (Fig. 5a) by fabricating 3 different electrodes and running DPV in 0.96 μM nicotine; a relative standard deviation of 1.16 shows that the
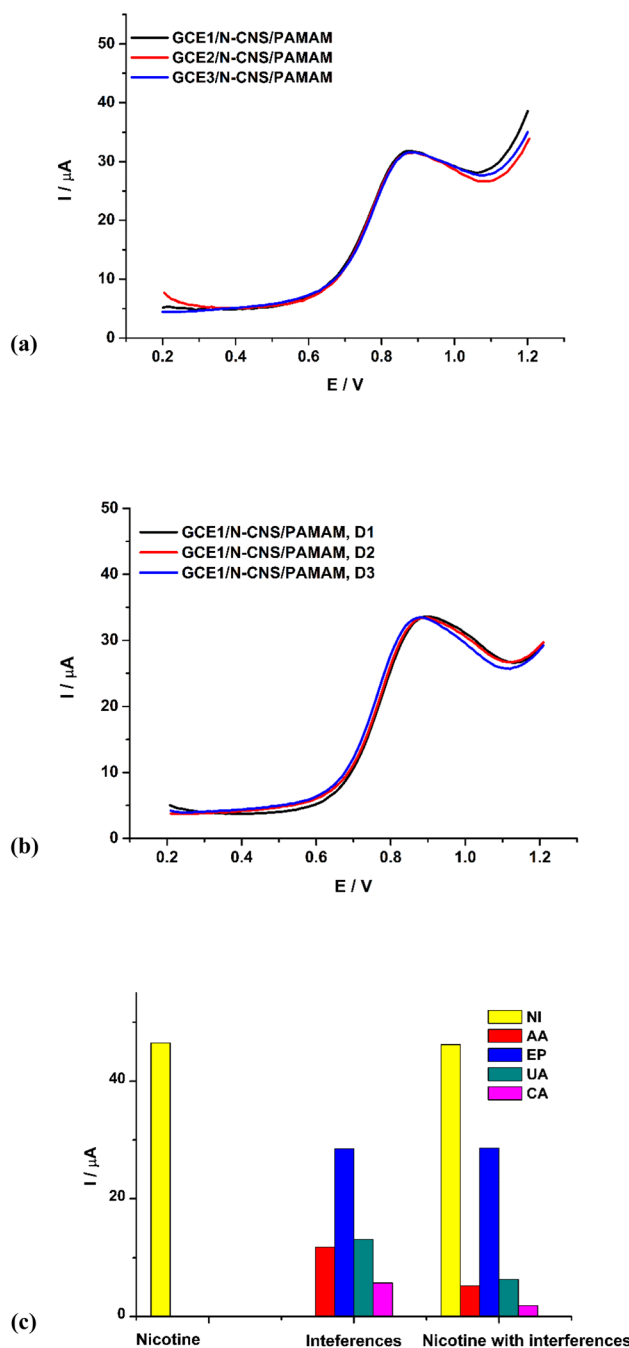
Fig. 5 (a) Reproducibility, (b) repeatability and (c) selectivity of GCE/N-CNS/PAMAM.

Table 3 Nicotine recoveries in flavoured hookah tobacco brands using GCE/N-CNS/PAMAM and UV-Vis

Sample	Spike/μM	GCE/N-CNS/PAMAM/μm	Nicotine mg g^{-1}	Recovery/%	RSD/%	UV-Vis/μm	Nicotine mg g^{-1}
Brand 1		43.51	0.35			43.39	0.35
	1.93	45.69	0.37	113	3.45	45.12	0.37
Brand 2		45.74	0.37			45.41	0.37
	1.93	47.58	0.39	121	2.79	47.55	0.39

sensor is reproducible. DPV was also employed to assess the sensor for repeatability (Fig. 5b), in three days by recleaning and refabricating the sensor the same way each day. The relative standard deviation of 0.76 proves that the method is repeatable. Lastly, the sensor was assessed for selectivity (Fig. 5c) in a wider potential window (−300 to 1600 mV) using four common chemicals that are likely to be found in the human body to replicate biological samples (such as blood, urine and serum), as the sensor will ultimately be used for nicotine measurement in humans. DPV analysis of GCE/N-CNS/PAMAM in 7.70 μM nicotine was first conducted in this window in the absence of interfering agents. The sensor was then applied in a mixture of 87.5 μM ascorbic acid (AA), epinephrine (EP), uric acid (UA), and caffeine (CA) in one electrolytic cell without nicotine. Subsequently, the sensor was applied in a mixture containing 77.77 μM interfering species and 6.85 μM nicotine and detection was conducted. The sensor was sensitive and selective for nicotine as the oxidation current for nicotine did not significantly change in the presence and absence of the interfering species, with no oxidation happening between 600 and 900 mV (nicotine oxidation potential) in the absence of nicotine. Furthermore, the sensor shows potential for multi-analysis, as it could detect all the interferents at their respective oxidation potentials.

3.6. Real sample application

Table 3 details the results of nicotine detected with the proposed method and verified using UV-Vis spectrometry. A quantity of 0.35–0.39 mg nicotine per gram of hookah pipe tobacco product was recovered at 113–121% accuracy and precision shown by the relative standard deviations of 2.79–3.45. This content varies per brand of hookah pipe tobacco as reported by Bakker and other scientists.[49]

4. Conclusion

We have demonstrated the application of a novel nanocomposite of nitrogen-doped carbon nanosheets and dendrimers in the development of an electrochemical sensor for nicotine. The sensor demonstrated a limit of detection of 0.05 μM nicotine in a linear concentration range of 1.93–61.64 μM with good reproducibility and selectivity. The sensor was applied in the detection of nicotine in flavoured hookah pipe tobacco. Hookah pipe tobacco smoking is becoming another route of nicotine abuse among young people in South Africa. Our sensor detected 0.35–0.39 mg g^{-1} of nicotine in flavoured hookah pipe tobacco. This suggests that hookah pipe smoking can be harmful considering the use of 20–50 g in whole night

sessions that happen in club scenes, depending on the brand as others have higher nicotine. Our result highlights that hookah pipe smoking may not be a safe alternative to cigarette smoking. Furthermore, the sensor lends itself to applications in drug abuse testing.

Data availability

The data supporting this article have been included as part of the ESI.†

Author contributions

Sesethu Makaluza: conceptualization, formal analysis, methodology, investigation, writing – original draft. Nyasha Midzi: methodology, writing – review and editing. Foluke O. G. Olorundare: methodology, visualization, writing – review and editing. Dimpo S. Sipuka: methodology, visualization, writing – review and editing. Tsholofelo I. Sebokolodi: methodology, visualization, writing – review and editing. Duduzile Nkosi: writing – review and editing. Omotayo A. Arotiba: conceptualization, methodology, visualization, supervision, project administration, funding acquisition, writing – review and editing.

Conflicts of interest

There are no conflicts to declare.

Acknowledgements

References

1 K. L. Sterling and R. Mermelstein, *Nicotine Tob. Res.*, 2011, **13**, 1202–1209.
2 D. Middha and A. Negi, *Egypt. J. Forensic Sci.*, 2019, **9**, 5.
3 M. Rezk-Hanna and N. L. Benowitz, *Nicotine Tob. Res.*, 2019, **21**, 1151–1161.
4 Z. Ben Taleb, A. Breland, R. Bahelah, M. E. Kalan, M. Vargas-Rivera, R. Jaber, T. Eissenberg and W. Maziak, *Nicotine Tob. Res.*, 2019, **21**, 1213–1219.

5 N. van der Merwe, T. Banoobhai, A. Gqweta, A. Gwala, T. Masiea, M. Misra and V. Zweigenthal, *S. Afr. Med. J.*, 2013, **103**, 847–849.

6 O. F. Khabour, K. H. Alzoubi, N. Al-Sawalha, M. B. Ahmad, A. Shihadeh and T. Eissenberg, *Life Sci.*, 2018, **200**, 110–114.

7 T. I. Sebokolodi, D. S. Sipuka, C. Muzenda, O. V. Nkwachukwu, D. Nkosi and O. A. Arotiba, *Chemosphere*, 2022, **303**, 2–3.

8 H. Holipah, H. W. Sulistomo and A. Maharani, *PLoS One*, 2020, **15**, 1–2.

9 N. D. Volkow and C. Blanco, *World Psychiatr.*, 2023, **22**, 203–229.

10 R. Jerome and A. K. Sundramoorthy, *Anal. Chim. Acta*, 2020, **1132**, 110–120.

11 D. S. Sipuka, O. A. Arotiba, T. I. Sebokolodi, T. R. Tsekeli and D. Nkosi, *Electroanalysis*, 2023, **35**, 1–2.

12 S. H. Kollins and R. A. Adcock, *Prog. Neuro-Psychopharmacol. Biol. Psychiatry*, 2014, **52**, 70–78.

13 S. Mihailescu and R. Drucker-Colín, *Arch. Med. Res.*, 2000, **31**, 131–144.

14 E. Small, H. P. Shah, J. J. Davenport, J. E. Geier, K. R. Yavarovich, H. Yamada, S. N. Sabarinath, H. Derendorf, J. R. Pauly, M. S. Gold and A. W. Bruijnzeel, *Psychopharmacology*, 2010, **208**, 143–158.

15 S. Krishnan-Sarin, S. S. O, B. G. Green and S.-E. G. Jordt Barry Green, *W. H. O. Tech. Rep. Ser.*, 2019, **1015**, 125–142.

16 A. Saljooqi, T. Shamspur and A. Mostafavi, *J. Mater. Sci.: Mater. Electron.*, 2020, **31**, 5471–5477.

17 G. Achilli, G. P. Cellermo, G. V. Melzi D'eril and F. Tagliaro, *J. Chromatogr. A*, 1996, **729**, 273–277.

18 M. El Hourani, S. Talih, R. Salman, N. Karaoghlanian, E. Karam, R. El Hage, N. A. Saliba and A. Shihadeh, *Chem. Res. Toxicol.*, 2019, **32**, 1235–1240.

19 X. Li, L. Liu, L. Guo, L. Xu, H. Kuang and C. Xu, *J. Pharm. Biomed. Anal.*, 2023, **223**, 1–2.

20 A. Karthika, P. Karuppasamy, S. Selvarajan, A. Suganthi and M. Rajarajan, *Ultrason. Sonochem.*, 2019, **55**, 196–206.

21 P. K. Lee and P. M. Woi, *J. Electroanal. Chem.*, 2019, **837**, 67–75.

22 G. Sridharan, K. L. Babu, D. Ganapathy, R. Atchudan, S. Arya and A. K. Sundramoorthy, *Crystals*, 2023, **13**, 1–32.

23 B. Yu, Y. Liu, J. Zhang, T. Hai, B. Li, P. Lu, H. Li, Y. Zhang, J. Yu, Z. Ye and Y. Jing, *Int. J. Electrochem. Sci.*, 2016, **11**, 4979–4987.

24 S. M. Fatemi, S. J. Fatemi and Z. Abbasi, *Polym. Bull.*, 2020, **77**, 6671–6691.

25 N. Soda and O. A. Arotiba, *Bioelectrochemistry*, 2017, **118**, 14–18.

26 Q. Liu, Y. Duan, Q. Zhao, F. Pan, B. Zhang and J. Zhang, *Langmuir*, 2014, **30**, 8238–8245.

27 M. K. Rybarczyk, E. Gontarek-Castro, K. Ollik and M. Lieder, *Processes*, 2021, **9**, 1–14.

28 V. Magesh, A. K. Sundramoorthy, D. Ganapathy, R. Atchudan, S. Arya, R. A. Alshgari and A. M. Aljuwayid, *Biosensors*, 2023, **13**, 1–3.

29 M. Stočes and I. Švancara, *Electroanalysis*, 2014, **26**, 2655–2663.

30 F. Aldeek, V. Lopez and J. H. Miller, *ACS Omega*, 2023, **8**, 31256–31264.

31 T. Xu, C. Wang, Z. Han and Y. Wang, *J. Mater. Sci.*, 2022, **57**, 8739–8751.

32 X. L. Zhang, C. N. Feng, H. P. Li and X. C. Zheng, *Cellulose*, 2021, **28**, 437–451.

33 M. Kirkby, A. H. Bin Sabri, A. Holmes, G. P. J. Moss and D. Scurr, *J. Pharm. Pharmacol.*, 2024, rgae080.

34 C. Ma, Q. Fan, M. Dirican, Y. Song, X. Zhang and J. Shi, *J. Mater. Sci.*, 2020, **55**, 16323–16333.

35 J. Qu, Q. Zhang, Y. Xia, Q. Cong and C. Luo, *Environ. Sci. Pollut. Res.*, 2015, **22**, 1408–1419.

36 E. Vasile, A. Serafim, D. Petre, D. Giol, P. Dubruel, H. Iovu and I. C. Stancu, *Sci. World J.*, 2014, **2014**, 103462.

37 M. A. Raj and S. A. John, *J. Phys. Chem. C*, 2013, **117**, 4326–4335.

38 I. Gallardo, J. Pinson and N. Vilà, *J. Phys. Chem. B*, 2006, **110**, 19521–19529.

39 D. A. Buttry, J. C. M. Peng, J.-B. Donnet and S. Rebouillat, *Carbon*, 1999, **37**, 1929–1940.

40 V. Uskoković, *Carbon Trends*, 2021, **5**, 1–3.

41 A. Sivanesan and S. A. John, *Electrochim. Acta*, 2009, **54**, 7458–7463.

42 O. A. Arotiba, J. H. Owino, P. G. Baker and E. I. Iwuoha, *J. Electroanal. Chem.*, 2010, **638**, 287–292.

43 F. Piazzolla and A. Temperini, *Tetrahedron Lett.*, 2018, **59**, 2615–2621.

44 P. Spieß, M. Berger, D. Kaiser and N. Maulide, *J. Am. Chem. Soc.*, 2021, **143**, 10524–10529.

45 P. W. Seavill and J. D. Wilden, *Green Chem.*, 2020, **22**, 7737–7759.

46 H. M. Özcan and M. K. Sezgintürk, *Biotechnol. Prog.*, 2015, **31**, 815–822.

47 X. Li, H. Zhao, L. Shi, X. Zhu, M. Lan, Q. Zhang and Z. Hugh Fan, *J. Electroanal. Chem.*, 2017, **784**, 77–84.

48 A. Varadwaj, P. R. Varadwaj and K. Yamashita, *J. Comput. Chem.*, 2018, **39**, 343–350.

49 I. M. E. Bakker-'T Hart, F. Bakker, J. L. A. Pennings, N. Weibolt, S. Eising and R. Talhout, *Tobac. Control*, 2023, **32**, 627–634.

50 Z. Su, S. Hu, Y. Xu, J. Liu, P. Liang, J. Wang, Q. Cao, Y. Peng, W. Zhang and D. Fan, *New J. Chem.*, 2024, **48**, 3370–3380.

51 L. Liv, *Electroanalysis*, 2024, **36**, e202400014.

52 G. Sridharan, K. L. Babu, D. Ganapathy, R. Atchudan, S. Arya and A. K. Sundramoorthy, *Crystals*, 2023, **13**, 589.

53 Y. Xue, Y. Wu, X. Zhang, J. Yan, Z. Long, F. Xi, D. Luo, Q. Liu, L. Guo, Y. Jing and L. Zhang, *Int. J. Electrochem. Sci.*, 2024, 100721.

54 M. Shehata, M. Zaki and A. M. Fekry, *Sci. Rep.*, 2023, **13**, 20432.

55 T. Leelasree, S. Goel and H. Aggarwal, *ACS Appl. Nano Mater.*, 2022, **5**, 16753–16759.